



Cite this: *Mater. Horiz.*, 2022, 9, 1479

Received 29th December 2021,
Accepted 28th February 2022

DOI: 10.1039/d1mh02073k

rsc.li/materials-horizons

A high-performance polarization-sensitive and stable self-powered UV photodetector based on a dendritic crystal lead-free metal-halide $\text{CsCu}_2\text{I}_3/\text{GaN}$ heterostructure†

Can Zou,^{‡a} Qing Liu,^{‡a} Kai Chen,^a Fei Chen,^a Zixuan Zhao,^a Yunxuan Cao,^a Congcong Deng,^a Xingfu Wang,^{id}^a Xiaohang Li,^b Shaobin Zhan,^{*c} Fangliang Gao,^{id}^{*a} and Shuti Li,^{id}^{*ad}

Polarization-sensitive photodetectors are the core of optics applications and have been successfully demonstrated in photodetectors based on the newly-emerging metal-halide perovskites. However, achieving high polarization sensitivity is still extremely challenging. In addition, most of the previously reported photodetectors were concentrated on 1D lead-halide perovskites and 2D asymmetric intrinsic structure materials, but suffered from being external bias driven, lead-toxicity, poor stability and complex processes, severely limiting their practical applications. Here, we demonstrate a high-performance polarization-sensitive and stable polarization-sensitive UV photodetector based on a dendritic crystal lead-free metal-halide $\text{CsCu}_2\text{I}_3/\text{GaN}$ heterostructure. By combining the anisotropic morphology and asymmetric intrinsic structure of CsCu_2I_3 dendrites with the isotropic material GaN film, a high specific surface area and built-in electric field are achieved, exhibiting an ultra-high polarization selectivity up to 28.7 and 102.8 under self-driving mode and -3 V bias, respectively. To our knowledge, such a high polarization selectivity has exceeded those of all of the reported perovskite-based devices, and is comparable to, or even superior to, those of the conventional 2D heterostructure materials. Interestingly, the unsealed device shows outstanding stability, and can be stored for over 2 months, and effectively maintained the performance even after repeated heating (373K)-cooling (300K) for different periods of time in ambient air, indicating a remarkable temperature tolerance and desired compatibility for applications under harsh conditions. Such excellent performance and simple method strongly show that the $\text{CsCu}_2\text{I}_3/\text{GaN}$ heterojunction photodetector has great potential in practical applications with high polarization-sensitivity. This work provides a new insight into designing novel high-performance polarization-sensitive optoelectronic devices.

New concepts

Recently, polarization-sensitive photodetectors have attracted great attention in the newly-emerging metal-halide perovskites due to their excellent optoelectronic features. However, the current reports based on perovskites mostly focus on materials with one-dimensional morphology that are subjected to an external bias, and there are few reports on materials with other morphologies. Herein, we demonstrate a high-performance polarization-sensitive and stable UV photodetector based on a dendritic crystal lead-free perovskite $\text{CsCu}_2\text{I}_3/\text{GaN}$ heterostructure. Benefiting from the anisotropic morphology and asymmetric intrinsic structure of CsCu_2I_3 dendrites and strong built-in electric fields, the device exhibits an ultra-high polarization selectivity up to 28.7 under self-driven mode and up to 102.8 under -3 V bias. More importantly, the present device, without any encapsulation or protection, can work efficiently after 2 months of storage in the open air. The excellent storage stability is superior to the performance of organic-inorganic hybrid perovskite-based devices. Such excellent performance and environmentally-friendly characteristics show that the proposed $\text{CsCu}_2\text{I}_3/\text{GaN}$ heterojunction photodetector has great potential in practical applications of highly polarization-sensitive and stable self-powered ultraviolet detection.

Introduction

Polarization-sensitive photodetectors have attracted great interest because of their significant applications, such as in high-contrast polarizers, optical switches and interconnects, *etc.*,^{1–6} which require photoactive materials with outstanding optoelectronic characteristics, and an anisotropic crystal structure or morphology.¹ However, most polarization-sensitive photodetectors still suffer from being external bias driven, low anisotropy ratio, complex processes and high costs,^{7–9} which greatly limits

^a Guangdong Engineering Research centre of Optoelectronic Functional Materials and Devices, Institute of Semiconductors, South China Normal University, Guangzhou, 510631, P. R. China. E-mail: gaofl@m.scnu.edu.cn

^b King Abdullah University of Science and Technology (KAUST), Advanced Semiconductor Laboratory, Thuwal 23955, Saudi Arabia

^c Shenzhen Institute of Information Technology, Innovation and Entrepreneurship School, Shenzhen, 518172, P. R. China. E-mail: 13266960452@163.com

^d 21C Innovation Laboratory, Contemporary Amperex Technology Ltd, Ningde, Fujian, 352100, P. R. China. E-mail: lishuti@scnu.edu.cn

† Electronic supplementary information (ESI) available. See DOI: 10.1039/d1mh02073k

‡ These authors contributed equally to this work.

their applications. There is an urgent need to explore materials with anisotropic structures or morphologies to obtain polarization-sensitive detectors with high anisotropy ratios. Recently, polarization-sensitive photodetectors based on metal halide materials have attracted much attention due to their inherent large light absorption coefficient and long charge diffusion length,^{10–16} and many advances have been witnessed.^{17–20} Polarized light detection was realized through the external anisotropy of the one dimensional (1D) geometric structure of perovskite nanowires (NWs), which have symmetrical crystal structures lacking inherent anisotropy. By using $\text{CH}_3\text{NH}_3\text{PbI}_3$ single crystal NWs, polarization-sensitive light detection was achieved by Su's groups.²¹ Zhang *et al.* also reported a polarization-dependent photodetector based on a CsPbX_3 single crystal NW array and achieved a photocurrent anisotropy ratio of 0.7 under an external bias.²² Furthermore, 1D morphology perovskites with asymmetric crystal structures were synthesized and polarization-sensitivity was realized. Ding *et al.* synthesized anisotropic crystal structure $\text{CH}_3\text{NH}_3\text{PbCl}_3$ perovskite NWs and revealed polarized light detection properties.²⁴ By using anisotropic orthogonal CsPbI_3 NWs, Zhou *et al.* fabricated a linearly polarized visible light detector with a photocurrent anisotropy ratio of 2.68.²³ However, the asymmetric crystal structure with 1D morphology still exhibits a low anisotropy ratio and is external bias driven. More recently, Luo *et al.* demonstrated a high-performance polarization-sensitive photodetector by using a two-dimensional (2D) anisotropic crystal structure $(4\text{-AMP})(\text{MA})_2\text{-Pb}_3\text{Br}_{10}$ combined with MAPbBr_3 film, which exhibited ultrahigh polarization selectivity up to 17.6 under a self-driven mode due to the strong built-in electric field.²⁵ But, up to now, most of the previous works used traditional lead-halide perovskites, and their environmental instability, toxicity and low polarization selectivity limit their further applications.^{26–29} In addition, the reported devices mainly focus on visible light/infrared light detection, and there are few reports on polarization-sensitive metal halide photodetectors in the ultraviolet (UV) region. Therefore, it is imperative to find an environmentally stable, high anisotropy ratio, and energy-saving lead-free alternative as a photoactive material for the ultraviolet region to solve the above problems.

Herein, we demonstrate a high-performance polarization-sensitive and stable UV heterostructure photodetector based on an anti-solvent processed dendritic crystal lead-free metal halide. By combining anisotropic morphology and asymmetric intrinsic structure CsCu_2I_3 dendrites with the isotropic material GaN film, the device exhibits an ultra-high polarization selectivity up to 28.7 under self-driven mode and up to 102.8 under -3 V bias. To our knowledge, such a high polarization selectivity exceeds those of all the reported perovskite-based polarization-sensitive devices, and is comparable to, or even superior to, those of conventional 2D heterostructure materials. Benefiting from high specific surface area and built-in electric field, the device performance is remarkable in terms of a photoresponsivity of 0.37 AW^{-1} , a specific detectivity of 1.83×10^{13} Jones, and a fast response speed of 7/8 ms under a low light density of $95 \mu\text{W cm}^{-2}$. Additionally, the device without encapsulation exhibits excellent working stability against thermal degradation in the

open air, indicating a remarkable temperature tolerance and desirable compatibility for applications under harsh conditions. Given the record polarization sensitivity and high stability, CsCu_2I_3 dendrites have the potential to be used in practical applications as high-performance polarization-sensitive ultraviolet photodetectors.

Results and discussion

Fig. 1a illustrates the synthesis procedures of the CsCu_2I_3 dendrites by using anti-solvent engineering, as reported in conventional lead halide perovskites, and methyl acetate was employed as the antisolvent. The morphology of the CsCu_2I_3 dendrites was examined by using scanning electron microscopy (SEM) and is shown in Fig. 1b. Fig. S1 (ESI[†]) shows the morphology of an individual CsCu_2I_3 dendritic crystal. A large number of pine-leaf-shaped microrods were observed, which reveals that the synthesized CsCu_2I_3 has a dendrite morphology. The energy dispersive X-ray spectroscopy (EDS) elemental mapping results (Fig. 1c) show that the Cs, Cu, and I elements are uniformly distributed. The EDS spectrum quantitative analysis shown in Fig. S2 (ESI[†]) further confirmed that the atomic ratio of Cs:Cu:I is 1:2.02:2.78, which is close to the stoichiometry of the CsCu_2I_3 material. Fig. 1d shows typical X-ray diffraction (XRD) patterns of the as-grown sample in comparison with the standard CsCu_2I_3 . A set of diffraction peaks at 10.72° , 13.42° , 21.62° , 26.14° , and 27.12° can be assigned to the (110), (020), (220), (221), and (040) planes of the orthorhombic CsCu_2I_3 .¹ No other impurity phases were found, further indicating the good crystallinity of the synthesis of CsCu_2I_3 dendrites. Fig. 1e shows the schematic crystal structure of orthorhombic CsCu_2I_3 dendrites, which is composed of a 1D chain structure formed by edge-sharing $[\text{CuI}_4]^-$ dimerized units. The Cs^+ ions are intercalated between the chains, which are coordinated by eight I^- ions in the form of double-capped trigonal prisms.³⁰ The crystal structures of CsCu_2I_3 from the top and left view indicate that CsCu_2I_3 has an anisotropic crystal structure, which provides the possibility of designing a polarization-sensitive photodetector by using its inherent anisotropic character. As shown in Fig. 1f, a clear absorption peak around 330 nm was observed, and the corresponding Tauc plot of the absorption spectrum (Fig. S3, ESI[†]) reveals that CsCu_2I_3 possesses a direct bandgap of 2.6 eV, which is similar to other articles.³¹ The red line displays the PL spectrum of CsCu_2I_3 dendrites at an excitation wavelength of 325 nm. An emission peak centered at 590 nm was observed, and the FWHM was 118 nm. Comparing its PL and absorption spectra, it should be mentioned that there is a large Stokes shift of ~ 260 nm. The large Stokes shift and broadband emission indicate that the PL emission cannot be simply attributed to the direct band emission, but also the exciton self-trapping.^{32,33} As shown in Fig. S4, (ESI[†]) due to strong photoacoustic coupling, the lower-energy self-trapped exciton (STE) states will capture free electrons, which will lead to the reorganization of the excited states. Fluorescence emission causes electrons to

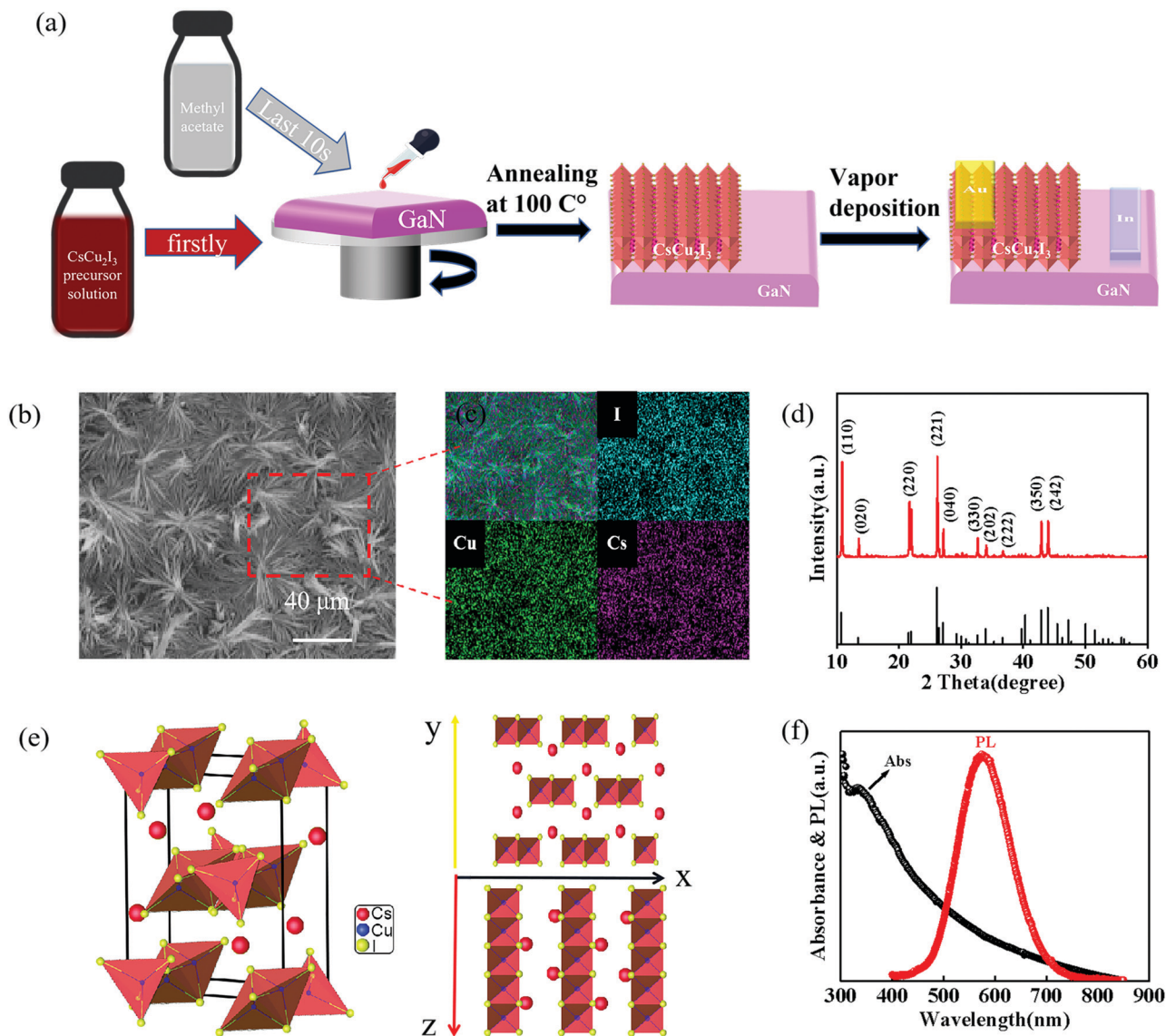


Fig. 1 (a) Schematic of the processing procedures of the CsCu₂I₃ dendrites. (b) SEM image of the CsCu₂I₃ dendrites. (c) EDS elemental mapping of the CsCu₂I₃ dendrites. (d) XRD patterns of the as-grown sample in comparison with the standard CsCu₂I₃. (e) Crystal structure of CsCu₂I₃ from side, top, and left views. (f) Steady-state PL and absorption spectra of the CsCu₂I₃ dendrites.

transition from the STE states to the ground states. Therefore, the Stokes shift is determined by the energy difference between the excited states and the STE states.

Fig. 2a displays the device structure of the fabricated CsCu₂I₃/GaN polarization-sensitive photodetector, in which 70 nm Au deposited on the CsCu₂I₃ dendrites serves as the cathode and 100 nm In deposited on the GaN film serves as the anode. The incident light is set to pass through the polarizer first, and then reflects to the photodetector. Therefore, the polarization state will not change as the propagation direction changes, and there will still be vibration components in the y direction (parallel to the built-in electric field). As presented in Fig. 2b, once the photogenerated electron-hole pairs diffuse into the hetero-interface, they can be quickly separated in opposite directions by the built-in electric field without an

external power supply. The holes will transport to the perovskite side, whereas the electrons will move to the opposite direction, generating photocurrent in the external circuit. Moreover, the built-in electric field is in a position to reduce the electron-hole recombination, favoring a low reverse dark current and thus improving the detectivity. In order to support the above statement of charge carrier transfer on the heterojunction surface, steady-state PL spectra of CsCu₂I₃ dendrites and the CsCu₂I₃/GaN heterostructure were measured. As shown in Fig. 2c, compared to the bare CsCu₂I₃ dendrites, the integrated PL intensity of the CsCu₂I₃/GaN heterostructure was reduced by ~30%, reflecting the transfer of photo-generated carriers from CsCu₂I₃ to GaN.³⁴ Fig. 2d shows a color mapping, which shows the variation of the PL intensity with the polarization angle. The minimum emission intensity near 590 nm is at the 0° angle

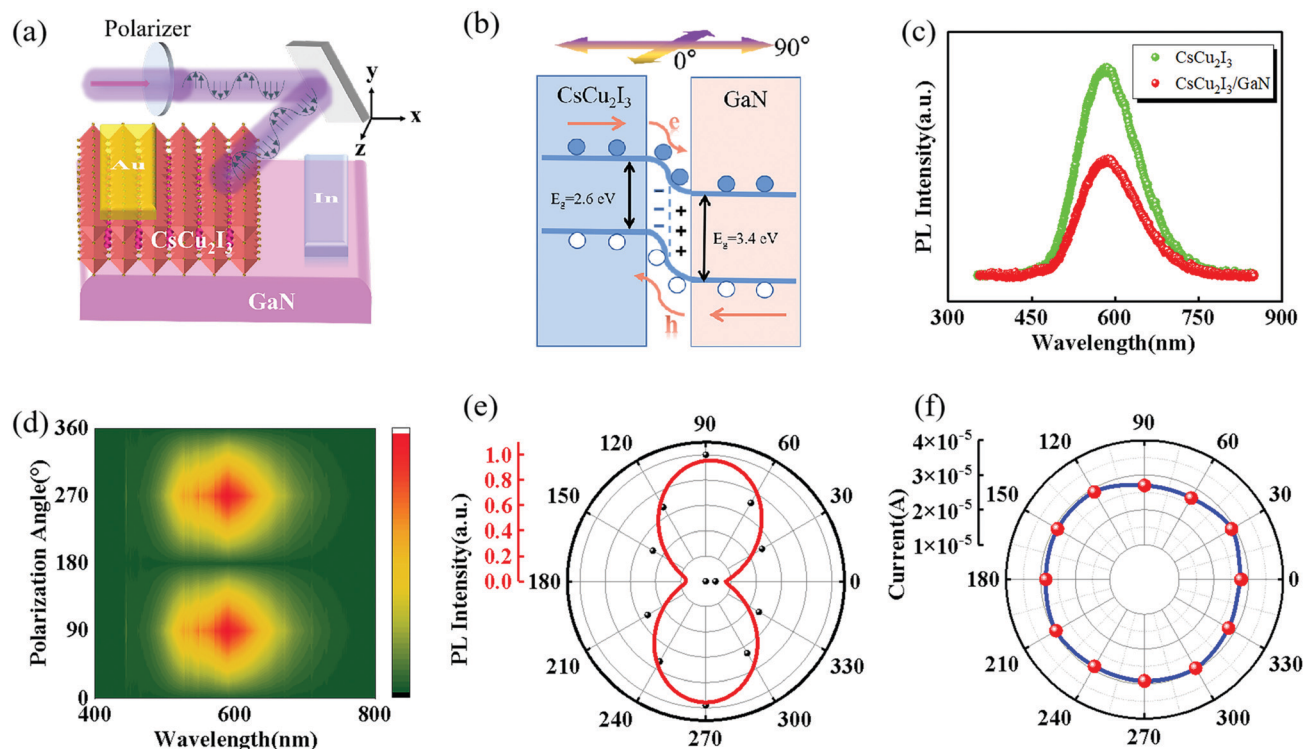


Fig. 2 (a) Schematic illustration of the $\text{CsCu}_2\text{I}_3/\text{GaN}$ heterojunction device. (b) Energy band diagrams of the $\text{CsCu}_2\text{I}_3/\text{GaN}$ heterojunction. (c) PL spectra of CsCu_2I_3 and the $\text{CsCu}_2\text{I}_3/\text{GaN}$ heterojunction. (d) PL spectra as a function of the incident light polarization. The color represents the emission intensity. (e) Polarization-dependent PL intensities of the $\text{CsCu}_2\text{I}_3/\text{GaN}$ heterojunction. (f) Polar plot of the angle-resolved photocurrent as a function of polarization angle of GaN measured at 325 nm under 3 V bias.

(0° is the z-axis marked in Fig. 2a), and its intensity gradually increases with the polarization angle and reaches the maximum at 90° polarization (y-axis). Furthermore, the red curve in Fig. 2e shows the cosine fit of the PL intensity with a period of 2π , and the PL intensity shows a polarization ratio of $\sim 2.6:1$. It should be noted that the polarization ratio here may be the contribution of the anisotropic crystal structure and the anisotropic morphology. This is similar to the report of Fang *et al.* on one-dimensional CsCu_2I_3 NWs.²⁷ And the polarization anisotropy ratio of pure CsCu_2I_3 dendrites is as high as 5 (as shown in Fig. S5, ESI†), which is better than that of 1D nanowires of 3.16. In contrast, the photocurrent of the GaN films exhibits a stable size with the transformation of the polarization angle, directly due to the isotropic crystal structure of GaN (Fig. 2f).

The above experimental results indicate that the $\text{CsCu}_2\text{I}_3/\text{GaN}$ heterostructure photodetector has UV polarization sensitivity. To further investigate its polarization sensitivity characteristics, we measured the photocurrent at the junction area as a function of incident light intensity and polarization angle, as shown in Fig. 3a. Obviously, the photocurrent exhibits significant anisotropy, and the photocurrent under 0° polarization angle is one to two orders of magnitude lower than that of the 90° angle. This is because when the polarized angle is parallel to the built-in electric field (incident along the y direction), the photo-generated carriers have the largest momentum in the direction of the built-in electric field,²⁵ which can effectively separate the generated electron-hole pairs and reduce their recombination.

Furthermore, Fig. 3b depicts a remarkable anisotropic photo-response of the photodetector *via* the 3D colormap within the bias from 0 to -3 V. Similar to the polarization-dependent PL spectra, the photocurrent increases with the increasing of the polarization angle and reaches the maximum at 90° polarization when the polarized light is incident along the y direction. Then, the photocurrent recovers totally at 180° polarization and is close to the 0° polarization photocurrent. This result was in good agreement with the sine function, which further demonstrated the polarization sensitivity of the $\text{CsCu}_2\text{I}_3/\text{GaN}$ heterostructure photodetector. The evolution of the current under zero bias was further extracted as a function of the polarization angle in polar coordinates, as plotted in Fig. 3c. A high photocurrent anisotropy ratio of about 28.7 was achieved (defined as the ratio of the measured photocurrent at 90° polarization to 0°), which is the maximum value among the perovskite-based polarized photodetectors as far as we know, and also superior to the other heterojunction materials, as summarized in Table 1. Besides, the evolution of the current under different bias voltages was also extracted as a function of the polarization angle in polar coordinates, as shown in Fig. 3d. Significantly, it is observed that the measured photocurrent is highly dependent on the polarization angle as well as bias voltage. Then, the variation of anisotropy ratio with voltage is shown in Fig. S6 (ESI†). It can be seen that the polarization selectivity obviously increases with the increasing of the bias voltage and an ultra-high polarization selectivity of 102.8 can be obtained under -3 V bias. Fig. 3e

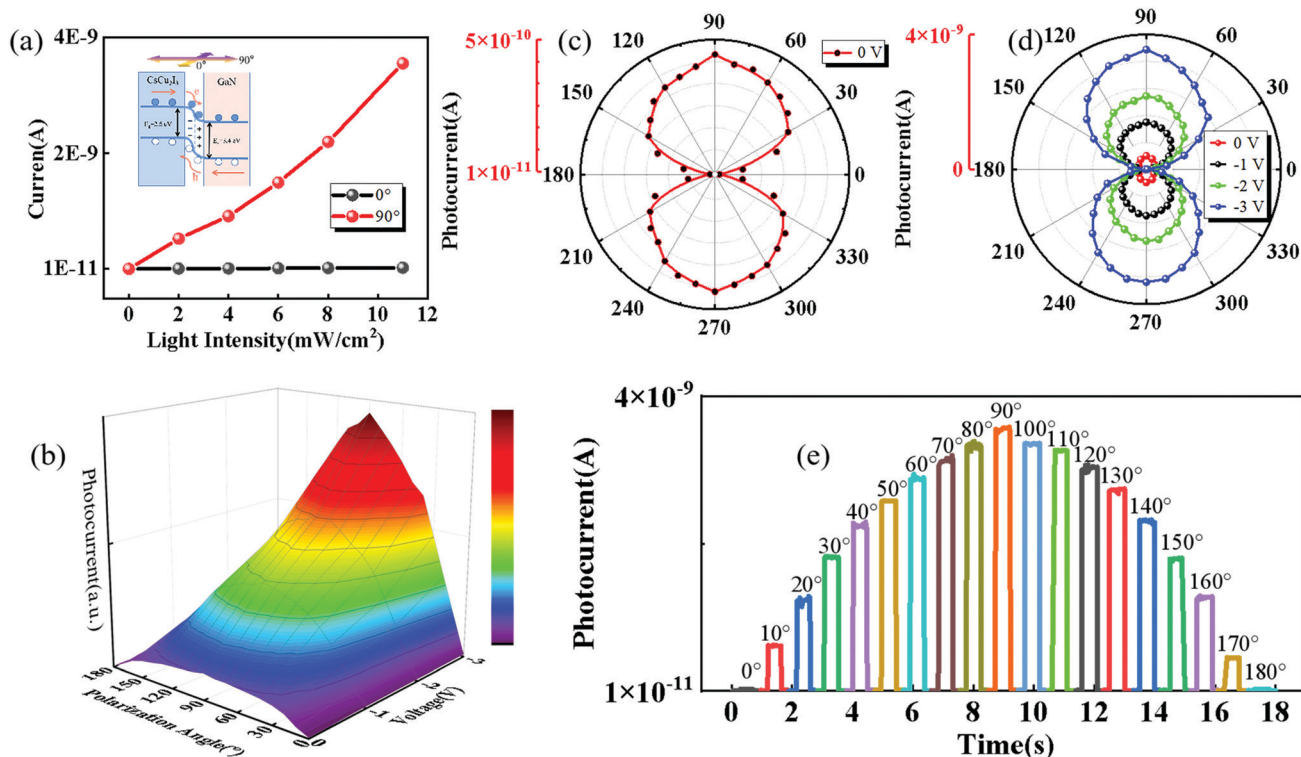


Fig. 3 (a) The variation of the photocurrent parallel and perpendicular to the interface of the heterostructure with the light intensity. (b) Anisotropic response in photocurrent under 325 nm light excitation described via the 3D colormap (photocurrent is denoted by the color bar). Polarization dependence of the photocurrent for the CsCu₂I₃/GaN heterostructure under different bias of (c) 0 V, and (d) 0 to −3 V. (e) Photocurrent response of the CsCu₂I₃/GaN heterostructure device under incident light with different polarization angles.

Table 1 Summary of the performance of the polarization-sensitive photodetectors

Device structure	Lead-free (yes/no)	Wavelength (nm)	Responsivity (AW ^{−1})	D^* ($\times 10^{12}$ Jones)	Polarization ratio	Ref.
CsCu ₂ I ₃ /GaN	Yes	300–350	0.37	18.3	28.7	This work
CsPbI ₃ nanowires	No	400–800	0.75	0.035	2.68	23
(BA) ₂ PbI ₄ nanowires	No	480–600	—	—	3.62	49
CH ₃ NH ₃ PbI ₃ nanowires	No	400–800	1000	—	2.6	21
(s-BA) ₂ (MA)Pb ₂ I ₇ crystal	No	610	0.097	0.279	1.16	50
CH ₃ NH ₃ PbCl ₃ crystal	No	350–450	0.0011	—	2.25	24
CsPbBr ₃ nanowires	No	400–530	0.0115	—	0.7	22
CsCu ₂ I ₃ nanowires	Yes	250–350	32.2	1.89	3.16	1
GeSe flake	Yes	400–950	—	—	2.16	52
Black phosphorus flake	Yes	400–3750	3.5×10^{-4}	—	3.5	6
GeAs/InSe	Yes	635	0.357	0.2	18	5
GeSe/MoS ₂	Yes	380–1046	0.1	0.014	2.95	48
SbI ₃ /Sb ₂ O ₃	Yes	450	—	0.001	3.14	51
(4-AMP)(MA) ₂ Pb ₃ Br ₁₀ /MAPbBr ₃	No	405	0.0015	0.038	17.6	25

depicts the corresponding I - t curves of the photodetector as a function of the polarization angle. A clear polarization dependence was observed, consistent with the above discussions.

Fig. S7 (ESI†) shows the I - V characteristics of the In/GaN/In and Au/CsCu₂I₃/Au devices in the dark and under UV light illumination. The near-linear I - V characteristics confirm that they make good ohmic contacts.⁵⁷ As can be seen from Fig. S7b, (ESI†) the dark current is about 0.003 μ A, and the current under 325 nm illumination is 0.097 μ A at a bias voltage of −5 V. A high $I_{\text{light}}/I_{\text{dark}}$ ratio of ~ 32 can be achieved at 325 nm.

The maximum value of 25.6 mA W^{−1} was achieved at a low light density of 0.05 mW cm^{−2} (Fig. S7c, ESI†). These results are close to those reported by Tang *et al.*³¹ It is worth noting that the existence of more grain boundaries in the horizontal direction increases the recombination loss of the photocurrent. But in the vertical direction, since the thickness of the synthesized CsCu₂I₃ dendrites is less than 1 μ m, and it can be observed from Fig. S1 (ESI†) that the CsCu₂I₃ dendrites are composed of a large number of one-dimensional single crystal microwires, the recombination loss in the vertical direction is much smaller

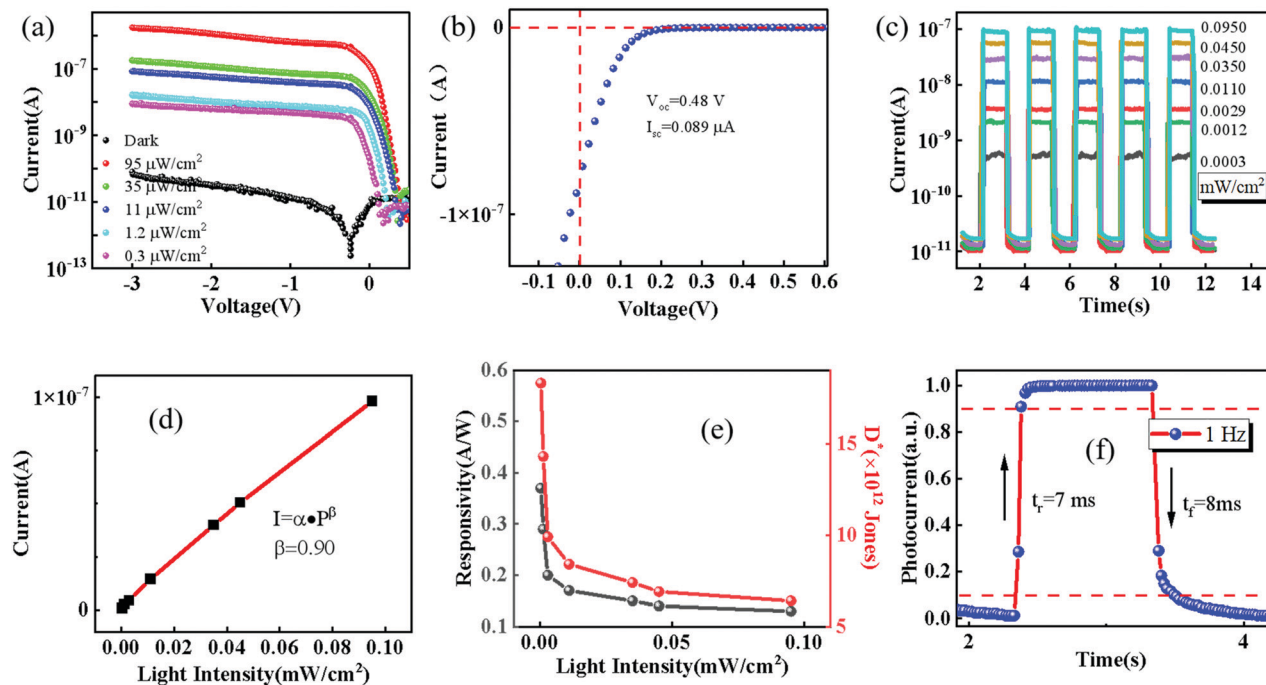


Fig. 4 (a) I - V curves of the photodetector tested in the dark and under different light irradiation intensity (325 nm). (b) Enlarged I - V curve showing the photovoltaic effect of the $\text{CsCu}_2\text{I}_3/\text{GaN}$ heterojunction. (c) Photocurrent response measured under 325 nm light excitation with varying intensity at zero bias. (d) Logarithmic plot of the photocurrent versus light irradiation power at zero bias. (e) Responsivity and detectivity of the photodetector versus light irradiation power. (f) Measurement of the τ_r and τ_f of the photodetectors at 1 Hz under zero bias.

than that in the horizontal direction. Finally, by combining the CsCu_2I_3 dendrites with the GaN film, benefiting from a high specific surface area and built-in electric field, the device exhibits good optoelectronic properties. Shown in Fig. 4a are the current-voltage (I - V) curves of the $\text{CsCu}_2\text{I}_3/\text{GaN}$ heterojunction photodetector under 325 nm UV illumination with varying light intensities (0.3 – $95 \mu\text{W cm}^{-2}$). Obviously, the current of the device at zero bias greatly increases from 1.02×10^{-11} A in the dark to 1.13×10^{-7} A under UV light ($95 \mu\text{W cm}^{-2}$). A short-circuit current (I_{sc}) of $0.089 \mu\text{A}$ and an open-circuit voltage (V_{oc}) of 0.48 V were obtained (Fig. 4b), showing a remarkable photovoltaic behavior. Fig. 4c shows the temporal photocurrent response of the device with different light intensities in self-powered mode. Apparently, the photocurrent increases gradually with the light intensity. And the photodetector can be stability switched reversibly between the on and off states, yielding an on/off ratio of 1.1×10^4 ($95 \mu\text{W cm}^{-2}$). Besides, it is worth noting that the on/off ratio of the photodetector can still reach 60 even under a low light irradiation of $0.3 \mu\text{W cm}^{-2}$, suggesting the excellent capability to detect a weak signal. The linear dynamic range (LDR) was estimated by using the expression³⁵

$$\text{LDR} = 20 \log \frac{I_{\text{p*}}}{I_{\text{d}}} \quad (1)$$

in which $I_{\text{p*}}$ represents the photocurrent, and I_{d} is the dark current. At zero bias, the LDR value was determined to be ~ 81 dB under $95 \mu\text{W cm}^{-2}$ light intensity, better than the state-of-the-art commercial photodetectors.³⁶ Furthermore, the

dependence of the photocurrent on the light intensity is shown in Fig. 4d. The data can be fitted well by the power law $I_{\text{p}} = \alpha \cdot P^{\beta}$. Where P is the light power, α represents a proportional constant, and β is an empirical value, which reflects the recombination of photoexcited carriers. The value of β is 0.90 in the experiment, close to that of an ideal photodetector ($\beta = 1$), which suggests a small recombination loss and high quality of the $\text{CsCu}_2\text{I}_3/\text{GaN}$ heterostructure. Furthermore, other device parameters, including the responsivity (R) and specific detectivity (D^*) of the heterojunction photodetector were calculated based on the following formulas

$$R = \frac{I_{\text{light}} - I_{\text{dark}}}{P_{\text{light}} S} \quad (2)$$

$$D^* = \frac{R \sqrt{S}}{\sqrt{2e} I_{\text{dark}}} \quad (3)$$

where I_{light} , I_{dark} , P_{light} , S and e are the photocurrent, dark current, incident light density, effective incident area ($7.85 \times 10^{-3} \text{ cm}^2$), and charge constant, respectively. With the above equations, values of R and D^* for the $\text{CsCu}_2\text{I}_3/\text{GaN}$ heterojunction photodetector were estimated at different light densities (Fig. 4e), and the maximum values of 370 mA W^{-1} and 1.83×10^{13} Jones were achieved at a low light density of $0.3 \mu\text{W cm}^{-2}$, respectively. Due to the increased carrier recombination probability at a higher light intensity, both values present a declining trend with increasing light intensity, consistent with other reports.^{37,38} Furthermore, the response speed of the $\text{CsCu}_2\text{I}_3/\text{GaN}$ photodetector was measured to evaluate its capability to

follow a varied optical signal. The schematic illustration is shown in Fig. S8a, (ESI†) in which a waveform generator was used to produce the pulsed light (1 Hz to 10 Hz), and an oscilloscope was used to record the change of photocurrent with time. Fig. S8b–d (ESI†) display the photoresponse to pulsed light with different modulation frequencies. And the obtained data were normalized relative to the photoresponse tested under 1 Hz pulsed light. It can be seen that the photodetector can work with remarkable reproducibility in a wide frequency range. As shown in Fig. 4f, the corresponding rise (τ_r , from 10 to 90% of the peak output photocurrent) and fall time (τ_f , from 90 to 10% of the peak output photocurrent) were estimated as 7 and 8 ms, respectively, which are comparable to those of many previously reported perovskite-based heterojunction photodetectors.^{39–41}

As we all know, the instability of conventional lead-halide perovskites is the main obstacle for their further applications in optoelectronic devices.^{42–45} Typically, lead-halide perovskites in moist air would decompose due to the hygroscopic amine salts, and even if the manufactured materials and devices are dried again, the chemical reaction process is irreversible. To evaluate the application potential of the dendritic crystal lead-free $\text{CsCu}_2\text{I}_3/\text{GaN}$ heterostructure photodetector, the investigation of its working stability is imperative. Fig. 5a shows the time-dependent light response of the device with 2000 cycles, which was tested in ambient air (27 °C, ~50% humidity) at a frequency of 2 Hz. One can observe that the photocurrent and the dark current of the photodetector can be well maintained after 2000 consecutive cycles, which indicates that the

prepared device has excellent repeatability even after being operated in ambient air without encapsulation. As shown in Fig. 5b, the as-grown CsCu_2I_3 dendrites maintain the structural integrity without decomposition after 2 months of storage in ambient conditions (27 °C, ~50% humidity). In addition to a slight change of the peak intensity, no other diffraction signals appear, proving higher stability against oxygen and water degradation than conventional lead-halide perovskites. Moreover, the original emission performance can be almost retained after 2 months of storage with the spectral shape unchanged, as shown in Fig. 5c. These results suggest that the Cu is ultra-stable in the unique CsCu_2I_3 dendrite crystal structure. In fact, the high air-stability property of the Cu-based halides was also observed previously in other Cu(I)-based halides, possibly owing to the robust chemical bonds between the Cu and halogen ions in such a unique dendrite crystal structure.^{53,54,56} All-inorganic halide perovskites and compounds are proved to be more thermally stable in higher temperatures due to the lack of numerous phase transitions.⁵⁵

In consideration of this, it is highly important to investigate the thermal stability of the CsCu_2I_3 dendrites. Fig. 5d displays that the device can still maintain a certain performance after repeated heating (373 K)-cooling (300 K) for different periods of time, demonstrating significant temperature tolerance for applications under harsh conditions. These results demonstrate good stability of the CsCu_2I_3 dendrites against heat, UV light, and environmental oxygen/moisture, and are also evidence of a reliable CsCu_2I_3 photoactive material compatible for practical applications. More importantly, the present device, without any

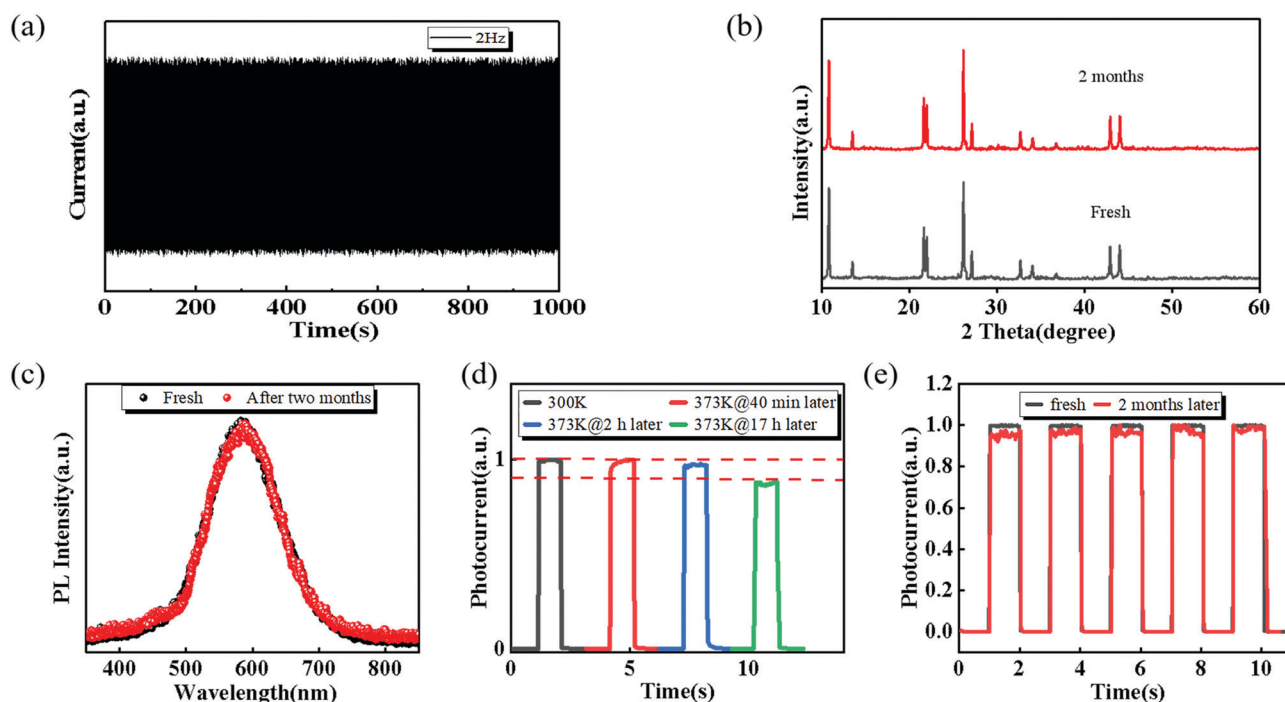


Fig. 5 (a) 2000 response cycles of the $\text{CsCu}_2\text{I}_3/\text{GaN}$ heterojunction photodetector. (b) The XRD, and (c) PL spectra evolution of the CsCu_2I_3 films after 2 months in ambient air. (d) The photocurrent after repeated heating–cooling for different periods of time. (e) Long-term storage stability of the photodetector in ambient air.

encapsulation and protection, can work efficiently after 2 months of storage in the open air (27 °C, ~50% humidity), and maintain almost the same photocurrent under the same test conditions (325 nm, 0.1 mW cm⁻²), as presented in Fig. 5e. The excellent storage stability is superior to the performance of organic-inorganic hybrid perovskite-based devices.^{46,47} The above observations suggest that the studied heterojunction photodetector has highly stable and reproducible characteristics, as well as good temperature resistance, rendering it potentially useful for the assembly of optoelectronic systems in the future.

Conclusions

In summary, a dendritic crystal metal-halide was successfully prepared by an anti-solvent engineering approach. By combining anisotropic morphology and asymmetric intrinsic structure CsCu₂I₃ dendrites with the isotropic material GaN film, we demonstrate a record-performance polarization selectivity up to 28.7 under self-driving mode and 102.8 under -3 V bias, which is the maximum value in metal halide-based polarized photodetectors, and is comparable to, or even better than, the conventional 2D heterostructure materials. Benefiting from a high specific surface area and built-in electric field, the device performance is remarkable in terms of a photoresponsivity of 0.37 A W⁻¹, a specific detectivity of 1.83×10^{13} Jones, and a fast response speed of 7/8 ms (95 μW cm⁻²). Moreover, the device without encapsulation exhibits excellent working stability against thermal degradation in the open air, and its detection performance can be effectively maintained even after repeated heating (373K)-cooling (300K) for different periods of time or being stored for 2 months in the open air, indicating a remarkable temperature tolerance and desired compatibility for applications under harsh conditions. Such excellent performance and simple method show that the proposed CsCu₂I₃/GaN heterojunction photodetector has great potential in the practical application of highly polarization-sensitive and stable self-powered ultraviolet detection.

Experimental section

GaN films were grown on sapphire substrates by metal-organic chemical vapor deposition (MOCVD), and were ultrasonically cleaned with ethanol, acetone, and deionized water, respectively. Next, the GaN film surfaces were treated with Ar gas plasma for 20 min. The CsCu₂I₃ dendrites were prepared using solution processing *via* a one-step spin-coating method. In detail, the precursor solution mixed with 1.0 mmol CsI (> 99.9%, Shanghai Aladdin Bio-Chem Technology Co.) and 2.0 mmol CuI (> 99.5%, Shanghai Aladdin Bio-Chem Technology Co.) in dimethyl sulfoxide (DMSO, > 99.8%, Shanghai Aladdin Bio-Chem Technology Co.) and *N,N*-dimethylformamide (DMF, > 99.9%, Shanghai Aladdin Bio-Chem Technology Co.) (completely dissolved at 60 °C for 4 h) was spin-coated on the prepared GaN substrate at 1500 rpm for 10 s and then 2000 rpm for 30 s, and 100 μL methyl acetate was dropped on the center of the spinning substrate at the last 10 s for

pinning the CsCu₂I₃ crystallization. The thickness of the films can be controlled by adjusting the speed and time of the spin-coating process. Following that, the sample was annealed at 100 °C for 1 h under Ar₂ conditions to evaporate the solvent and enhance the crystallization.

For device preparation, an In electrode (100 nm) on GaN and an Au electrode (70 nm) on the CsCu₂I₃ dendrites were prepared by thermal evaporation by using a shadow mask. The morphology of the prepared CsCu₂I₃ dendrites was tested by field-emission SEM (ZEISS Ultra 55). The XRD measurement was conducted using a Panalytical X'Pert Pro. The absorption spectra were recorded using a UV-vis spectrometer (Varian Cary 500). Photoluminescence (PL) spectra were acquired *via* a 325 nm He-Cd laser and collected at room temperature. All photoelectric performance characteristics of the PDs were monitored using a precision source/measure unit (model B2902, Keysight Technologies, Inc.), and all the measurements were performed under ambient conditions.

Author contributions

Shuti Li and Fangliang Gao guided and supervised the research. Can Zou carried out the characterizations and wrote the manuscript. Qing Liu and Shaobin Zhan designed and participated in the experiments. Kai Chen, Fei Chen, Zixuan Zhao, Yunxuan Cao, Congcong Deng, Xiaohang Li and Xingfu Wang assisted the experimental analysis. All authors discussed the results and reviewed the manuscript.

Conflicts of interest

There are no conflicts to declare.

Acknowledgements

This work is supported by the Key-Area Research and Development Program of Guangdong Province (Grant No. 2020B010174004), the National Natural Science Foundation of China (Grant No. 61874161, 11804103 and 52002135), Guangdong Natural Science Foundation for Distinguished Young Scholars (2018B030306048), Education Department Project Foundation Program of Guangdong, Province of China (Grant No. 2017KZDXM002), Featured Innovation Projects of Colleges and Universities in Guangdong Province (Natural Science, No. 2018KTSCX233, 2018KTSCX232 and 2019KTSCX033), Science and Technology Program of Guangzhou, China (Grant No. 202002030033), Natural Science Foundation of Guangdong Province, China (Grant No. 2018A030313395), and 21C Innovation Laboratory, Contemporary Ampere Technology Ltd (Grant No. 21C-OP-202109).

Notes and references

- 1 Y. Li, Z. Shi, L. Wang, Y. Chen, W. Liang, D. Wu, X. Li, Y. Zhang, C. Shan and X. Fang, *Mater. Horiz.*, 2020, 7, 1613–1622.
- 2 M. Long, A. Gao, P. Wang, H. Xia, C. Ott, C. Pan, Y. Fu, E. Liu, X. Chen, W. Lu, T. Nilges, J. Xu, X. Wang, W. Hu and F. Miao, *Sci. Adv.*, 2017, 3, 1700589.

- 3 V. Martin, B. Boy, L. Norman, O. Kenichiro, K. N. Seemantini and E. B. Brett, *Optica*, 2018, **5**, 1329–1337.
- 4 J. Zhang, J. Zhao, Y. Zhou, Y. Wang, K. S. Blankenagel, X. Wang, M. Tabassum and L. Su, *Adv. Opt. Mater.*, 2021, **9**, 2100524.
- 5 S. Amol, L. Xiangyang, P. Vladimir, G. Gabor, K. Masaru, X. Huili and J. Debdeep, *Nano Lett.*, 2007, **7**, 2999–3006.
- 6 X. Wang, A. M. Jones, K. L. Seyler, V. Tran, Y. Jia, H. Zhao, H. Wang, L. Yang, X. Xu and F. Xia, *Nat. Nanotechnol.*, 2015, **10**, 517–521.
- 7 X. Jingxian, S. Yiming, W. Liangwei, W. Weizhe, G. Wei, H. Nengjie and L. Jingbo, *Adv. Opt. Mater.*, 2021, **9**, 2101017.
- 8 Z. Wang, P. Luo, B. Han, X. Zhang, S. Zhao, S. Wang, X. Chen, L. Wei, S. Yang, X. Zhou, S. Wang, X. Tao and T. Zhai, *ACS Nano*, 2021, **15**, 20442–20452.
- 9 J. Wang, M. S. Gudiksen, X. Duan, Y. Cui and C. M. Lieber, *Science*, 2001, **293**, 1455–1457.
- 10 X. Geng, F. Wang, H. Tian, Q. Feng, H. Zhang, R. Liang, Y. Shen, Z. Ju, G.-Y. Gou, N. Deng, Y.-T. Li, J. Ren, D. Xie, Y. Yang and T.-L. Ren, *ACS Nano*, 2020, **14**, 2860–2868.
- 11 L. Li, S. Ye, J. Qu, F. Zhou, J. Song and G. Shen, *Small*, 2021, **17**, 2005606.
- 12 H.-P. Wang, S. Li, X. Liu, Z. Shi, X. Fang and J.-H. He, *Adv. Mater.*, 2021, **33**, 2003309.
- 13 H. Wang, R. Haroldson, B. Balachandran, A. Zakhidov, S. Sohal, J. Y. Chan, A. Zakhidov and W. Hu, *ACS Nano*, 2016, **10**, 10921–10928.
- 14 F. Wang, X. Zou, M. Xu, H. Wang, H. Wang, H. Guo, J. Guo, P. Wang, M. Peng, Z. Wang, Y. Wang, J. Miao, F. Chen, J. Wang, X. Chen, A. Pan, C. Shan, L. Liao and W. Hu, *Adv. Sci.*, 2021, **8**, 2100569.
- 15 D. H. Chun, Y. J. Choi, Y. In, J. K. Nam, Y. J. Choi, S. Yun, W. Kim, D. Choi, D. Kim, H. Shin, J. H. Cho and J. H. Park, *ACS Nano*, 2018, **12**, 8564–8571.
- 16 C. Lan, H. Zou, L. Wang, M. Zhang, S. Pan, Y. Ma, Y. Qiu, Z. L. Wang and Z. Lin, *Adv. Mater.*, 2020, **32**, 2005481.
- 17 Z. Shi, S. Li, Y. Li, H. Ji, X. Li, D. Wu, T. Xu, Y. Chen, Y. Tian, Y. Zhang, C. Shan and G. Du, *ACS Nano*, 2018, **12**, 1462–1472.
- 18 M.-C. Yen, C.-J. Lee, K.-H. Liu, Y. Peng, J. Leng, T.-H. Chang, C.-C. Chang, K. Tamada and Y.-J. Lee, *Nat. Commun.*, 2021, **12**, 4460.
- 19 H. Cong, X. Chu, F. Wan, Z. Chu, X. Wang, Y. Ma, J. Jiang, L. Shen, J. You and C. Xue, *Small Methods*, 2021, **5**, 2100517.
- 20 H. Wang, L. Li, J. Ma, J. Li and D. Li, *J. Mater. Chem. C*, 2021, **9**, 11085–11090.
- 21 J. Feng, X. Yan, Y. Liu, H. Gao, Y. Wu, B. Su and L. Jiang, *Adv. Mater.*, 2017, **29**, 1605993.
- 22 Y. Gao, L. Zhao, Q. Shang, Y. Zhong, Z. Liu, J. Chen, Z. Zhang, J. Shi, W. Du, Y. Zhang, S. Chen, P. Gao, X. Liu, X. Wang and Q. Zhang, *Adv. Mater.*, 2018, **30**, 1801805.
- 23 Y. Zhou, J. Luo, Y. Zhao, C. Ge, C. Wang, L. Gao, C. Zhang, M. Hu, G. Niu and J. Tang, *Adv. Opt. Mater.*, 2018, **6**, 1800679.
- 24 J. Ding, X. Cheng, L. Jing, T. Zhou, Y. Zhao and S. Du, *ACS Appl. Mater. Interfaces*, 2018, **10**, 845–850.
- 25 X. Zhang, L. Li, C. Ji, X. Liu, Q. Li, K. Zhang, Y. Peng, M. Hong and J. Luo, *Natl. Sci. Rev.*, 2021, **8**, nwab044.
- 26 Z.-Z. Ma, Z.-F. Shi, L.-T. Wang, F. Zhang, D. Wu, D.-W. Yang, X. Chen, Y. Zhang, C.-X. Shan and X.-J. Li, *Nanoscale*, 2020, **12**, 3637–3645.
- 27 Y. Li, Z. Shi, W. Liang, L. Wang, S. Li, F. Zhang, Z. Ma, Y. Wang, Y. Tian, D. Wu, X. Li, Y. Zhang, C. Shan and X. Fang, *Mater. Horiz.*, 2020, **7**, 530–540.
- 28 M. Wang, W. Wang, B. Ma, W. Shen, L. Liu, K. Cao, S. Chen and W. Huang, *Nano-Micro Lett.*, 2021, **13**, 62.
- 29 B. Yang and K. Han, *Acc. Chem. Res.*, 2019, **52**, 3188–3198.
- 30 Q. Li, Z. Chen, B. Yang, L. Tan, B. Xu, J. Han, Y. Zhao, J. Tang and Z. Quan, *J. Am. Chem. Soc.*, 2020, **142**, 1786–1791.
- 31 J. Yang, W. Kang, Z. Liu, M. Pi, L.-B. Luo, C. Li, H. Lin, Z. Luo, J. Du, M. Zhou and X. Tang, *J. Phys. Chem. Lett.*, 2020, **11**, 6880–6886.
- 32 Z. Ma, Z. Shi, D. Yang, Y. Li, F. Zhang, L. Wang, X. Chen, D. Wu, Y. Tian, Y. Zhang, L. Zhang, X. Li and C. Shan, *Adv. Mater.*, 2021, **33**, 2001367.
- 33 S. Cheng, A. Beitlerova, R. Kucerkova, E. Mihokova, M. Nikl, Z. Zhou, G. Ren and Y. Wu, *ACS Appl. Mater. Interfaces*, 2021, **13**, 12198–12202.
- 34 J. Ma, X. Xia, S. Yan, Y. Li, W. Liang, J. Yan, X. Chen, D. Wu, X. Li and Z. Shi, *ACS Appl. Mater. Interfaces*, 2021, **13**, 15409–15419.
- 35 Y. Liu, Y. Zhang, K. Zhao, Z. Yang, J. Feng, X. Zhang, K. Wang, L. Meng, H. Ye, M. Liu and S. Liu, *Adv. Mater.*, 2018, **30**, 1707314.
- 36 Z. Shi, Y. Li, S. Li, X. Li, D. Wu, T. Xu, Y. Tian, Y. Chen, Y. Zhang, B. Zhang, C. Shan and G. Du, *Adv. Funct. Mater.*, 2018, **28**, 1707031.
- 37 C.-Y. Wu, Z. Wang, L. Liang, T. Gui, W. Zhong, R.-C. Du, C. Xie, L. Wang and L.-B. Luo, *Small*, 2019, **15**, 1900730.
- 38 C. Fang, H. Wang, Z. Shen, H. Shen, S. Wang, J. Ma, J. Wang, H. Luo and D. Li, *ACS Appl. Mater. Interfaces*, 2019, **11**, 8419–8427.
- 39 K.-L. Chu, C.-H. Chen, S.-W. Shen, C.-Y. Huang, Y.-X. Chou, M.-Y. Liao, M.-L. Tsai, C.-I. Wu and C.-C. Chueh, *Chem. Eng. J.*, 2021, **422**, 130112.
- 40 H. Cong, X. Chu, F. Wan, Z. Chu, X. Wang, Y. Ma, J. Jiang, L. Shen, J. You and C. Xue, *Small Methods*, 2021, **5**, 2100517.
- 41 C. Jia, X. Huang, D. Wu, Y. Tian, J. Guo, Z. Zhao, Z. Shi, Y. Tian, J. Jie and X. Li, *Nanoscale*, 2020, **12**, 4435–4444.
- 42 Z. Shi, Y. Li, Y. Zhang, Y. Chen, X. Li, D. Wu, T. Xu, C. Shan and G. Du, *Nano Lett.*, 2017, **17**, 313–321.
- 43 F. Zhang, S. Huang, P. Wang, X. Chen, S. Zhao, Y. Dong and H. Zhong, *Chem. Mater.*, 2017, **29**, 3793–3799.
- 44 W. Tian, H. Zhou and L. Li, *Small*, 2017, **13**, 1702107.
- 45 Z. Ma, Z. Shi, C. Qin, M. Cui, D. Yang, X. Wang, L. Wang, X. Ji, X. Chen, J. Sun, D. Wu, Y. Zhang, X. J. Li, L. Zhang and C. Shan, *ACS Nano*, 2020, **14**, 4475–4486.
- 46 K. Aitola, K. Domanski, J.-P. Correa-Baena, K. Sveinbjörnsson, M. Saliba, A. Abate, M. Grätzel, E. Kauppinen, E. M. J. Johansson, W. Tress, A. Hagfeldt and G. Boschloo, *Adv. Mater.*, 2017, **29**, 1606398.
- 47 J. Yang, Q. Hong, Z. Yuan, R. Xu, X. Guo, S. Xiong, X. Liu, S. Braun, Y. Li, J. Tang, C. Duan, M. Fahlman and Q. Bao, *Adv. Opt. Mater.*, 2018, **6**, 1800262.

- 48 Y. Xin, X. Wang, Z. Chen, D. Weller, Y. Wang, L. Shi, X. Ma, C. Ding, W. Li, S. Guo and R. Liu, *ACS Appl. Mater. Interfaces*, 2020, **12**, 15406–15413.
- 49 D. Ghoshal, T. Wang, H.-Z. Tsai, S.-W. Chang, M. Crommie, N. Koratkar and S.-F. Shi, *Adv. Opt. Mater.*, 2019, **7**, 1900039.
- 50 X. Li, D. Li, Y. Peng, Y. Liu, J. Wang, L. Li, Y. Yao, X. Liu and J. Luo, *J. Mater. Chem. C*, 2021, **9**, 9499–9504.
- 51 M. Xiao, H. Yang, W. Shen, C. Hu, K. Zhao, Q. Gao, L. Pan, L. Liu, C. Wang, G. Shen, H.-X. Deng, H. Wen and Z. Wei, *Small*, 2020, **16**, 1907172.
- 52 X. Wang, Y. Li, L. Huang, X.-W. Jiang, L. Jiang, H. Dong, Z. Wei, J. Li and W. Hu, *J. Am. Chem. Soc.*, 2017, **139**, 14976–14982.
- 53 X. Mo, T. Li, F. Huang, Z. Li, Y. Zhou, T. Lin, Y. Ouyang, X. Tao and C. Pan, *Nano Energy*, 2021, **81**, 105570.
- 54 P. Cheng, L. Sun, L. Feng, S. Yang, Y. Yang, D. Zheng, Y. Zhao, Y. Sang, R. Zhang, D. Wei, W. Deng and K. Han, *Angew. Chem., Int. Ed.*, 2019, **58**, 16087–16091.
- 55 D. Li, G. Wang, H.-C. Cheng, C.-Y. Chen, H. Wu, Y. Liu, Y. Huang and X. Duan, *Nat. Commun.*, 2016, **7**, 11330.
- 56 Z. Li, Z. Li, Z. Shi and X. Fang, *Adv. Funct. Mater.*, 2020, **30**, 2002634.
- 57 W. Song, J. Chen, Z. Li and X. Fang, *Adv. Mater.*, 2021, **33**, 2101059.